Evaluation of Cloud Microphysics in JMA-NHM Simulations Using Bin or Bulk Microphysical Schemes through Comparison with Cloud Radar Observations

TAKAMICHI IGUCHI,[*,+] TERUYUKI NAKAJIMA,[#] ALEXANDER P. KHAIN,[@] KAZUO SAITO,[&] TOSHIHIKO TAKEMURA,[**] HAJIME OKAMOTO,[**] TOMOAKI NISHIZAWA,[++] AND WEI-KUO TAO[+]

[*] Earth System Science Interdisciplinary Center, University of Maryland, College Park, Maryland
[+] Laboratory for Atmospheres, NASA Goddard Space Flight Center, Greenbelt, Maryland
[#] Atmosphere and Ocean Research Institute, The University of Tokyo, Kashiwa, Japan
[@] Department of Atmospheric Sciences, Institute of the Earth Science, The Hebrew University of Jerusalem, Jerusalem, Israel
[&] Meteorological Research Institute, Tsukuba, Japan
[**] Research Institute for Applied Mechanics, Kyushu University, Fukuoka, Japan
[++] National Institute for Environmental Studies, Tsukuba, Japan

(Manuscript received 9 August 2011, in final form 16 March 2012)

ABSTRACT

Numerical weather prediction (NWP) simulations using the Japan Meteorological Agency Nonhydrostatic Model (JMA-NHM) are conducted for three precipitation events observed by shipborne or spaceborne W-band cloud radars. Spectral bin and single-moment bulk cloud microphysics schemes are employed separately for an intercomparative study. A radar product simulator that is compatible with both microphysics schemes is developed to enable a direct comparison between simulation and observation with respect to the equivalent radar reflectivity factor Ze, Doppler velocity (DV), and path-integrated attenuation (PIA). In general, the bin model simulation shows better agreement with the observed data than the bulk model simulation. The correction of the terminal fall velocities of snowflakes using those of hail further improves the result of the bin model simulation. The results indicate that there are substantial uncertainties in the mass–size and size–terminal fall velocity relations of snowflakes or in the calculation of terminal fall velocity of snow aloft. For the bulk microphysics, the overestimation of Ze is observed as a result of a significant predominance of snow over cloud ice due to substantial deposition growth directly to snow. The DV comparison shows that a correction for the fall velocity of hydrometeors considering a change of particle size should be introduced even in single-moment bulk cloud microphysics.

1. Introduction

Active remote sensing using radar/lidar is useful for observing the degree of density of clouds and precipitation. W-band cloud radars for frequencies ranging from 75 to 111 GHz can observe small particles that are several micrometers in diameter, such as cloud droplets, with strong Rayleigh scattering; these particles cannot be detected by C-band or X-band precipitation radars. A frequency of approximately 94 GHz in W-band radar measurements is commonly used to monitor clouds and precipitation because of the small attenuation by atmospheric gas absorption at this frequency (Lhermitte 1987). Many observations using ground-based, shipborne, or airborne W-band radars have been reported by prior studies (e.g., Clothiaux et al. 1995). Furthermore, *Cloud-Sat*, equipped with a 94-GHz Cloud Profiling Radar (CPR), was launched in April 2006, and its data continue to be compiled (Stephens et al. 2002, 2008). Global observation by A-Train satellites, including *CloudSat*, provides significant information about the structures of clouds and precipitation. Another project, the EarthCARE mission, is currently being prepared; both 94-GHz Doppler radar and lidar will be loaded on the satellite. It is therefore timely to make a study using datasets from cloud radar observations.

The validation of cloud modeling is a way to make use of the measurements of cloud radars. The majority of prior studies have used radar-signal simulation packages, such as QuickBeam (Haynes et al. 2007), to calculate an equivalent radar reflectivity factor Ze from prognostic variables, which corresponded to the actually measured

Ze; this approach enables a direct signal-based comparison. For example, the global output of a multiscale modeling framework (MMF) was compared with *Cloud-Sat* CPR observations (Marchand et al. 2009). In a simulation of the Madden–Julian oscillation (MJO) using a global cloud-resolving model (GCRM) with a horizontal grid size of several kilometers, measurements of tropical clouds and precipitation were compared with datasets from the *CloudSat* CPR and Tropical Rainfall Measuring Mission Precipitation Radar (TRMM PR) (Miura et al. 2007; Masunaga et al. 2008) as well as remote sensing data from the *Cloud–Aerosol Lidar and Infrared Pathfinder Satellite Observation* (*CALIPSO*)/*CloudSat* satellites (Inoue et al. 2010; Satoh et al. 2010). The global distributions and structures of clouds and precipitation in the Met Office global model were evaluated using *CloudSat* CPR data (Bodas-Salcedo et al. 2008). The vertical structures of midlatitude and tropical clouds observed using shipborne radar and lidar were compared with those simulated by the Center for Climate System Research–National Institute for Environmental Studies (CCSR–NIES) atmospheric general circulation model (AGCM) (Okamoto et al. 2007, 2008). The radar reflectivity and Doppler velocity of arctic mixed-phase clouds simulated by a three-dimensional cloud-resolving model coupled with spectral bin microphysics were compared with measurements by a millimeter cloud radar (Fan et al. 2009).

In this study, we conducted numerical weather prediction (NWP) simulations using the Japan Meteorological Agency Nonhydrostatic Model (JMA-NHM) and compared the results with observations by shipborne or spaceborne cloud radars for three specific midlatitude cases. Spectral-bin-microphysics and single-moment-bulk schemes for clouds were separately used for an intercomparison study. The corresponding variables in the measurement products, such as Ze, Doppler velocity (DV), and path-integrated attenuation (PIA), were calculated using a newly developed radar product simulator that had been optimized for the bin scheme. This approach may allow a signal-based comparison between simulated data and observed data (Masunaga et al. 2010). The assumptions in the simulator are highly consistent with those made in the model microphysical schemes. Our simulator directly utilizes particle size distributions (PSDs) of hydrometeors resulting from the bin model simulations. Built-in PSDs, assumed originally in the bulk microphysics, are introduced into the simulator when applied to the bulk model simulations.

In the first case, data of a 95-GHz Doppler radar on a research vessel during a cruise over the Pacific Ocean near Japan in May 2001 were used. The second and third cases involved cloud systems that occurred near Japan in

November 2006 that were recorded by *CloudSat* global observation using the 94-GHz CPR. Comparative analyses of the three cases may provide a better understanding of the differences between the simulated and observed data, despite the differences in the weather conditions and locations, because the zenith and nadir remote sensing data are complementary to each other with differing attenuation profiles.

The methodology is described in section 2 and includes a description of the NWP simulation and an explanation of the radar product simulator and radar observations. The comparative analysis between the numerical experiments and the observed data is described in section 3. The summary and conclusions are presented in section 4.

2. Methodology

a. Cloud radar observations

1) MR01/K02 CRUISE OF THE RESEARCH VESSEL *MIRAI*

The MR01/K02 research cruise was conducted with a shipborne 95-GHz Doppler radar and lidar with a zenith looking over the northwest Pacific near Japan from 14 to 28 May 2001 (Sugimoto et al. 2002; Okamoto et al. 2007). The observed data provided Ze, linear depolarization ratio (LDR), DV, and the correlation coefficient between the horizontal and vertical polarization signals; the technical description can be found in Horie et al. (2000). The calibration accuracy of the radar signal is approximately ±1 dB (Okamoto 2002; H. Kuroiwa 2001, personal communication). The vertical range of the data reaches a height of approximately 12 km with intervals of 82.5 m and a time interval of 1 min. This study targets 22 and 23 May 2001, when the vessel stayed at approximately 34°N, 146°E, and a low pressure system typical of the midlatitudes with associated fronts approached from the west and passed over the vessel (Fig. 1a). The radar observed the vertical structures of the clouds and the precipitation attributed to the low pressure and frontal system. The passing clouds were altostratus, nimbostratus, and shallow cumulus.

2) *CLOUDSAT* CPR OBSERVATION

CloudSat is a polar-orbiting satellite with a mean equatorial altitude of 705 km in the formation of the five satellites known as the A-Train constellation (Stephens et al. 2002, 2008). The vertical interval of the CPR data is 240 m, and the horizontal cross-track and along-track resolutions are 1.4 and 1.8 km, respectively. The Ze in the *CloudSat* Geometric Profile (2B-GEOPROF) product (Mace et al. 2007; Marchand et al. 2008; Stephens et al. 2008; Tanelli et al. 2008) and the PIA due to
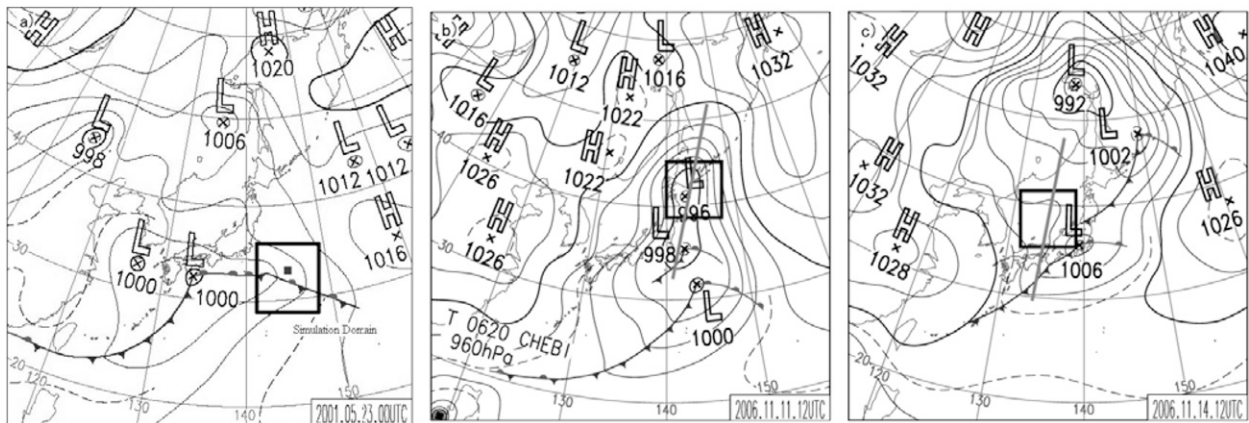
FIG. 1. Surface weather charts at (a) 0000 UTC 23 May 2001, (b) 1200 UTC 11 Nov 2001, and (c) 1200 UTC 14 Nov 2001 with overlaid black squares corresponding to the simulation domains. The dots and lines denote the coordinates of *Mirai* and the footprints of *CloudSat*, respectively. (The surface weather charts are provided by the Japan Meteorological Agency.)

hydrometeors in the Precipitation Column (2C-PRECIP-COLUMN) product (Haynes et al. 2009) were provided from the *CloudSat* Data Processing Center (DPC).

We analyzed two events, when *CloudSat* passed over clouds near Japan on 11 and 14 November 2006 under dissimilar weather conditions and in different regions. The corresponding *CloudSat* track granules were numbered 2873 and 2917 by the *CloudSat* DPC. In the first case, the satellite passed over the northeastern part of Japan at approximately 1638 UTC 11 November 2006 from 34.6°N, 141.7°E to 46.1°N, 145.7°E (the latitude and longitude boundaries follow those of the QuickLook segment provided by the DPC). The CPR observed very thick nimbostratus and precipitation located near the center of a low pressure system in the mature stage (Fig. 1b). A uniform vertical structure of reflectivity extended from 39° to 46°N along the footprint of the satellite. In the second case, the satellite passed over the Japan Sea at roughly 1708 UTC 14 November 2006 from 34.6°N, 134.0°E to 46.1°N, 137.6°E. The CPR observed the structures of shallow convective clouds extending behind a cold front over the sea surface (Fig. 1c).

b. Description of JMA-NHM

The operational version of JMA-NHM (Saito et al. 2006) is the main model framework for three-dimensional NWP simulations. The basic governing equations are fully compressive nonhydrostatic equations. The time-splitting horizontally explicit and vertically implicit (HE-VI) scheme is used to inhibit the inflation of sound waves. The Arakawa-C and Lorenz grid structures are employed in the horizontal and vertical grid discretizations, respectively. For points that differed from the original JMA-NHM, the broadband radiative transfer code "mstrn-x" (Sekiguchi and Nakajima 2008) was employed to calculate

atmospheric radiation. The subgrid convective parameterization scheme in the JMA-NHM was not employed to prevent a conflict with the spectral bin scheme, which is described below.

The spectral bin microphysics scheme, which is based on the module package of the Hebrew University Cloud Model (HUCM; e.g., Khain et al. 2000), is integrated into the JMA-NHM (Iguchi et al. 2008). Hydrometeors are categorized into one water class and six ice classes [i.e., water droplets, ice crystals (plate, column, dendrite), snowflakes, graupel, and hail]. Ice crystals are defined as primary ice particles that have not coagulated with any other hydrometeor particles; snowflakes are aggregates of ice crystals. Graupel and hail are rimed particles that primarily arise from the combination of supercooled droplets and ice hydrometeor particles or from the freezing of supercooled droplets. Snowflakes, graupel, and hail are assumed to be spheres when calculating their microphysics (Khain and Sednev 1995). The discrete PSDs of hydrometeors are represented on a grid containing 33 doubling mass bins[1] covering particles mass sizes in a range in which $3.35 \times 10^{-11} < m < 1.44 \times 10^{-1}$ g ($2 < r < 3251$ μm in terms of the radii of droplets or melted ice). The scheme calculates nucleation for droplets and ice crystals, condensation and deposition growths, evaporation, sublimation, droplet freezing, melting, and coalescence growth. The ice nucleation rate was updated using the equation in Cotton et al. (1986).

Additional experiments using the bin scheme were conducted together: the fall velocities of snowflakes were replaced with those of hail. This adjustment was

---

[1] The sequence of particle mass is a geometric progression with common ratio 2.

adopted from the latest update of the bin microphysics (Khain et al. 2011), in which the fall velocities of snowflakes are variable because of riming effects. This type of adjustment for the fall velocity of snow was tested to ameliorate the discrepancy between the model simulations and radar observations in several prior studies (Fan et al. 2009; Li et al. 2010).

The bulk microphysical scheme originally included in the JMA-NHM was also integrated to allow a comparative analysis. This scheme is a single-moment bulk accounting for explicit classes, two of water and three of ice: cloud water, rain, cloud ice, snow, and graupel (Lin et al. 1983; Ikawa and Saito 1991; Eito and Aonashi 2009). The amount of cloud water is calculated using an instantaneous saturation adjustment. The autoconversion rate of rain from cloud water is calculated by Kessler's autoconversion formula through the collision and coalescence of droplets. Cloud ice is defined as pristine ice crystals, and snow is defined as snow crystals or aggregates. Graupel is a type of rimed ice particle that includes hail. Exponential distribution functions are assumed to capture the forms of the PSDs of rain, snow, and graupel. Monodispersive functions are hypothesized to characterize cloud water and cloud ice. The gravitational sedimentations of particles categorized as cloud water and cloud ice are not calculated because of their tiny terminal velocities.[2]

c. Setup of the NWP simulations using JMA-NHM

Three sets of NWP simulations were prepared separately for 22–23 May 2001, 11 November 2006, and 14 November 2006 (hereinafter, the three cases are referred to as M2223, C2873, and C2917). The simulation domains for M2223, C2873, and C2917 were centered at 34°N, 146°E; 42°N, 143°E; and 38°N, 135°E, respectively. The simulation domains for all the cases had a horizontal scale of 600 km with a grid interval size of 3 km. The vertical grid component up to a height of 22 600 m was divided into 40 layers with intervals increasing from 40 to 1120 m with altitude. A time step of 20 s was set; a variable time step shorter than this interval was used for the bin microphysics.

In the case of M2223, nine individual NWP simulations with 6 h of integration were conducted for 54 h in total from 1800 UTC 21 May to 0000 UTC 24 May 2001. Each simulation transferred the specific prognostic variables [i.e., potential temperature, mixing ratio of vapor, and PSDs of hydrometeor particles and condensation nuclei (CN)] to the next 6-h simulation. We continuously sampled the prognostic variables in the column over the horizontal

---

grid nearest to the coordinates of the vessel per 1 min during 22 and 23 May. In the cases of C2873 and C2917, the pairs of two individual simulations with 6 h of integration were conducted for 12 h in total from 0600 to 1800 UTC on 11 and 14 November 2006, respectively. We sampled the prognostic variables in the columns over the nearest horizontal grids to the footprints of *CloudSat* at 1638 UTC 11 November and at 1708 UTC 14 November.

To set the initial and lateral boundary conditions of the specific prognostic variables (i.e., the two components of horizontal velocities, potential temperature, and mixing ratio of the water vapor), the JMA mesoanalysis dataset (JMA-MANAL) distributed by the Japan Meteorological Business Support Center (JMBSC) was employed in NWP simulations. This dataset had a horizontal grid interval of 10 km, 20 pressure-plane levels, and 4 (for 2001) and 8 (for 2006) samples per day. The National Centers for Environmental Prediction (NCEP) reanalysis data, which had a horizontal resolution of T62 Gaussian grid and four samples per day, were used to set the sea surface temperature (SST). A one-way nesting technique for CN was applied for the bin model simulations (Iguchi et al. 2008). The CN fields were calculated from the spectral radiation transport model for aerosol species [the Spectral Radiation Transport Model for Aerosol Species (SPRINTARS); e.g., Takemura et al. 2005] coupled with the CCSR–NIES AGCM (Hasumi and Emori 2004), with a horizontal resolution of T106 Gaussian grid, 20 vertical layers, and 1 sample per day.

d. Radar product (Ze, Doppler velocity, and PIA) simulator

A radar product simulator was used to convert the prognostic variables obtained from the NWP simulations to a corresponding product of radar measurement. The prognostic variables in the sampled columns are interpolated on the vertical layers of the radar measurements before the calculation of the radar simulator. Our simulator is based on that developed for comparing shipborne radar/lidar measurements with AGCM simulations (Okamoto et al. 2007, 2008). The simulator was modified so that it could be plugged into both the bin and bulk microphysics of JMA-NHM. The assumptions in the simulator (i.e., PSD and particle fall velocities) are consistent with those made in the model microphysical schemes.

The equivalent radar reflectivity factor is calculated using the following equation (Okamoto et al. 2003):

$$\text{Ze} = \frac{\lambda^4}{\pi^5 |K|^2} \left[\int_{r_{\min}}^{r_{\max}} \frac{dn(r)}{dr} C_{\text{bk}}(r) \, dr \right], \qquad (1)$$

where λ is the wavelength, r is the radius of particles, $n(r)$ is the number concentration of particles with a radius less

than r, and C_{bk} is the backscattering cross section given from the lookup table that was precalculated on the basis of the discrete dipole approximation (DDA) approach. Also, K is the dielectric factor estimated from $\tilde{n}$ by $|K| = |(\tilde{n}^2 - 1)/(\tilde{n}^2 + 2)|$, where $\tilde{n}$ is the complex refractive index. The value of $|K|$ is set to be 0.828 for the *Mirai* case (Horie et al. 2000; Okamoto et al. 2007) and 0.75 for the *CloudSat* case (Stephens et al. 2008). The different K values are derived from their respective equations to convert the received power to Ze. Here $|K|$ is assumed to be the same for both water and ice; this assumption is based on the definition of Ze for each observation. We use the logarithmic form, dBZe $= 10 \log_{10}$Ze, expressed in terms of decibels (dB), in the following analysis.

The backscattering cross sections of all ice hydrometeor particles were calculated using the DDA approach regardless of their effective or bulk densities in the cloud microphysical schemes. The mass equivalent volume with a density of 0.9 g cm^{-3} was defined for each mass bin, and the backscattering cross section was computed using DDA for the sphere particle with the equivalent volume (Okamoto 2002; Okamoto et al. 2003; Sato and Okamoto 2006). The sensitivity of the result of the radar simulator to spherical and nonspherical particle models in the DDA computation is briefly discussed in subsection 3a.

The prognostic PSDs of the hydrometeors in the bin model simulation are directly substituted for Eq. (1). In the case of the bulk model simulation, the corresponding PSDs are calculated using the prognostic mixing ratios and built-in PSDs assumed originally in the bulk microphysics; then, the PSDs are directly substituted for Eq. (1), as in the case of the bin model simulation. The total mass concentration is conserved when the PSDs are expanded on the bins. The built-in PSDs of rain, snow, and graupel are assumed to be exponential distributions in the bulk microphysics in the following way:

$$N(D) = N_0 \exp(-\Lambda D), \qquad (2)$$

where D is the particle diameter, N_0 is the intercept parameter (i.e., $N_{r0} = 8.0 \times 10^6$ m^{-4} for rain, $N_{s0} = 1.8 \times 10^6$ m^{-4} for snow, and $N_{g0} = 1.1 \times 10^6$ m^{-4} for graupel; Ikawa and Saito 1991), and Λ is the slope parameter determined by the mass mixing ratio with the equations of Lin et al. (1983). The particle densities, $\rho_r = 1.0 \times 10^3$ kg m^{-3} for rain, $\rho_s = 8.4 \times 10^1$ kg m^{-3} for snow, and $\rho_g = 3.0 \times 10^2$ kg m^{-3} for graupel (Eito and Aonashi 2009), are assumed to calculate the slope parameters. The PSDs of cloud water and cloud ice are assumed to be monodispersive distributions in the bulk microphysics, and their diameters are defined in the following form:
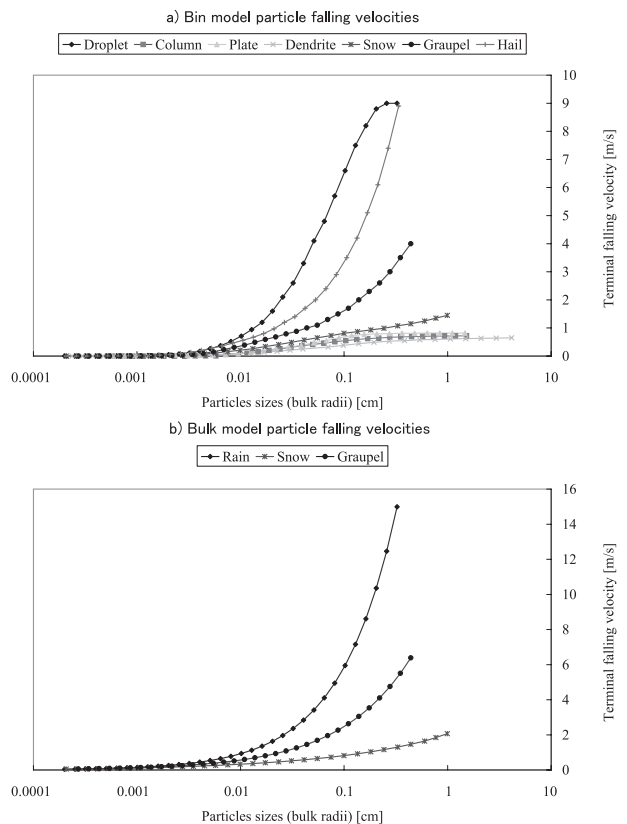

FIG. 2. Relationships between the terminal fall velocities at 1000 hPa and the bulk radii of cloud particles in (a) the bin and (b) the bulk microphysics.

$$\overline{D} = \left[\frac{6q\rho_a}{\pi N_0 \rho}\right]^{1/3}, \qquad (3)$$

where q is the mixing ratio and ρ_a is the air density. The prescribed number concentrations are $N_{0c} = 1.0 \times 10^8$ m^{-3} for cloud water (Ikawa and Saito 1991) and $N_{0i} = 2.0 \times 10^6 \times \exp(-0.122T)$ m^{-3} for cloud ice (T is the temperature in degrees Celsius) (Wilson and Ballard 1999; Bodas-Salcedo et al. 2008) (this alternative parameter for cloud ice was used because no assumption was made in the original). The particle densities are $\rho_c = 1.0 \times 10^3$ kg m^{-3} for cloud water and $\rho_i = 5.0 \times 10^2$ kg m^{-3} for cloud ice.

The attenuation due to atmospheric hydrometeors for Ze is calculated in the following way:

$$\text{Ze}_H = \text{Ze} \times \exp(-2\tau), \qquad (4)$$

where τ is the optical thickness, that is, the integral of the extinction coefficient at the radar wavelength from the radar to the target, expressed as (e.g., Kikuchi et al. 2006):

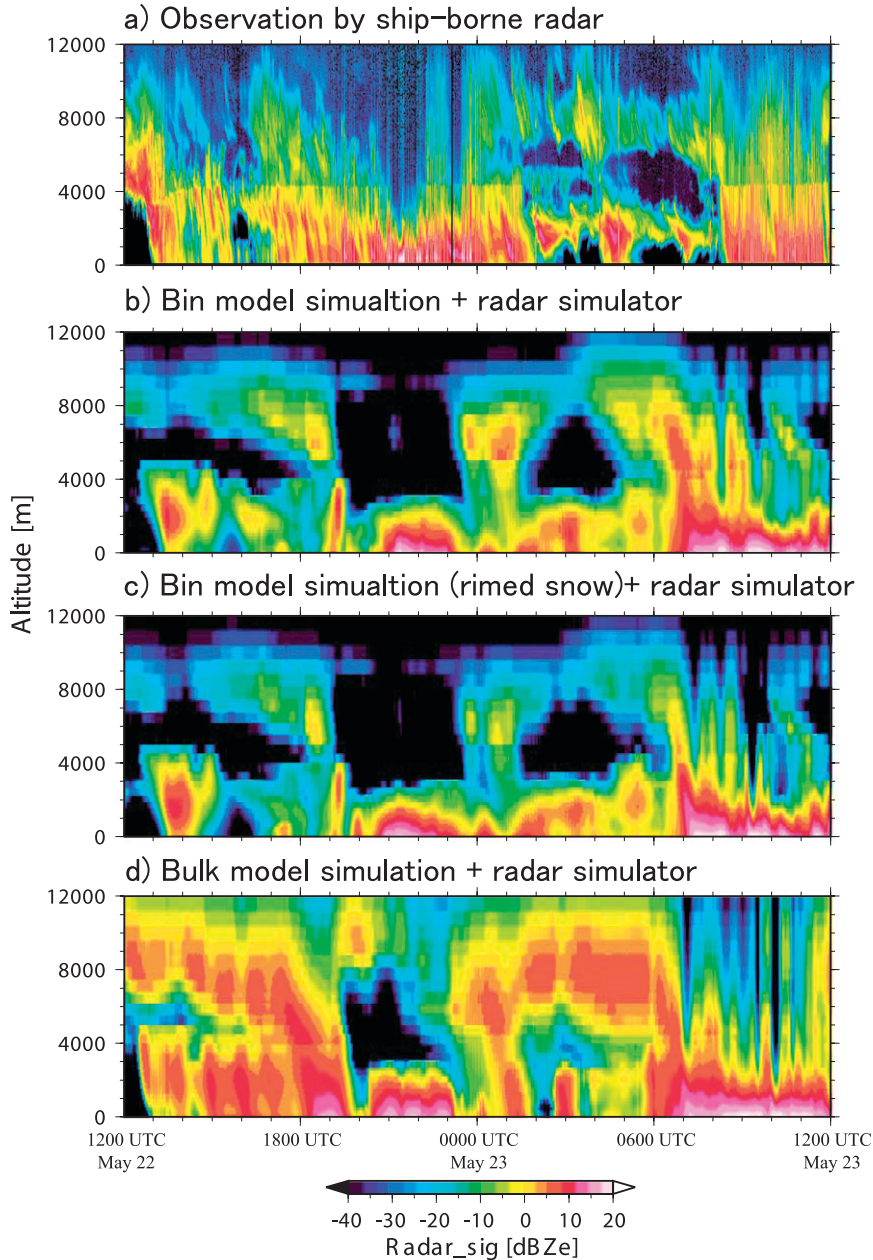$$\tau = \int_{z_r}^{z_t} \int_{r_{min}}^{r_{max}} n(r) C_{ext}(r) \, dr \, dz, \qquad (5)$$

FIG. 3. Time–height cross sections (THCSs) of the equivalent radar reflectivity factor (dBZe) (a) measured by the 95-GHz Doppler radar onboard *Mirai*, and calculated by the radar product simulator applied to the outputs of (b) the bin (control), (c) the bin with the terminal fall velocities of snow equalized to those of hail in all size bins (virtually rimed snow), and (d) the bulk model simulations from 1200 UTC 22 May to 1200 UTC 23 May 2001.

where the C_{ext} values are the extinction cross sections of the hydrometeor particles. Also, z_r and z_t are the heights of the radar and the target, respectively; the heights of the radars are the surface in a shipborne observation case and 705 km aloft in a spaceborne case. The attenuation resulting from the atmospheric hydrometeor components was modeled in the simulator; that is, we used radar-measured Ze values without the

attenuation correction in our comparative analyses. The PIA due to hydrometeors is calculated as the two-way integrated extinction (Haynes et al. 2009) by multiplying τ by 2 and $10/\ln(10)$.

Gas absorption for the typical atmosphere at mid-latitude regions is simply parameterized using the calculation result in Hogan and Illingworth (1999). The total two-way gas attenuation between space and surface
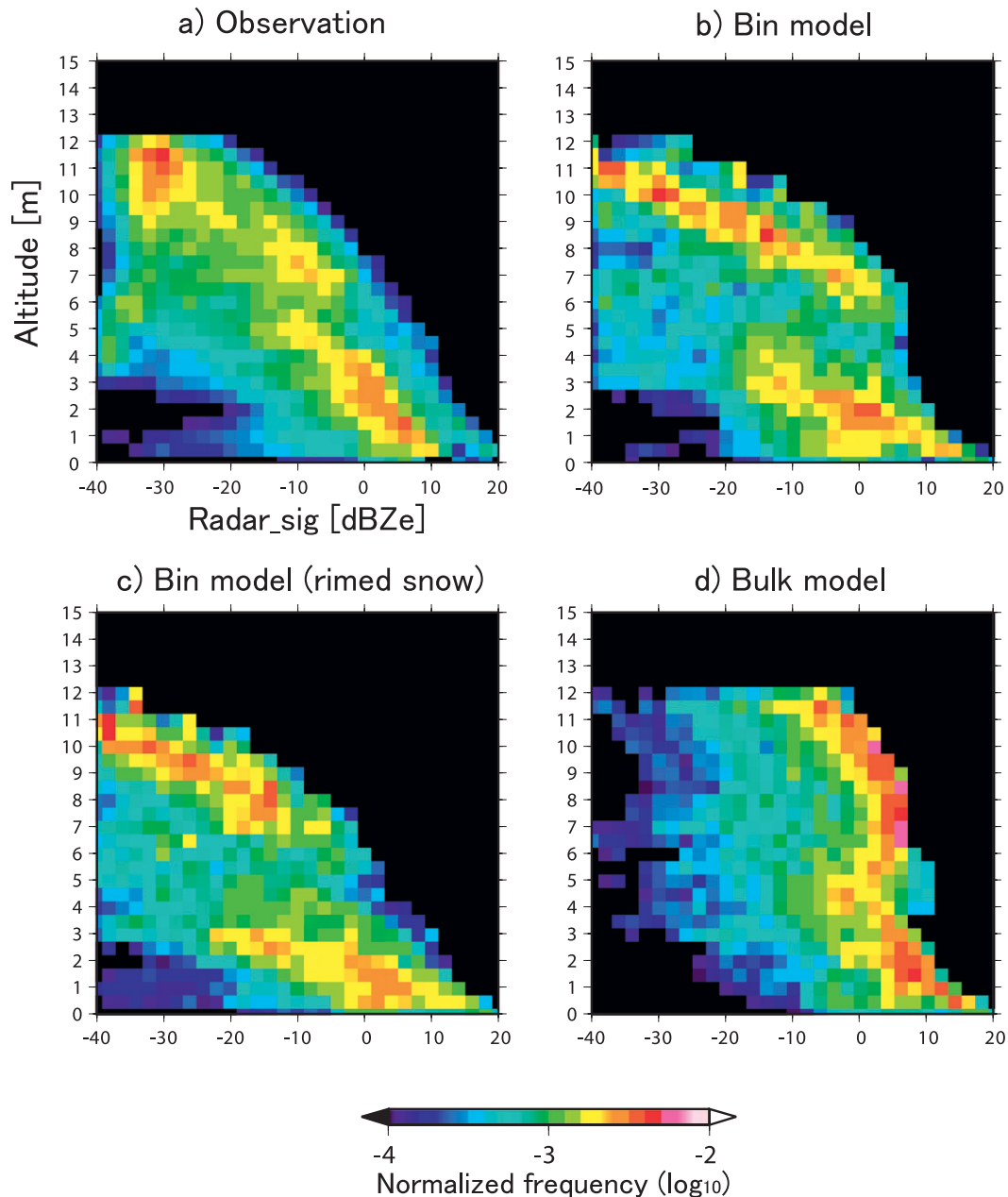
FIG. 4. Normalized dBZe–height histograms constructed (a) from the radar measurement and from the simulations by (b) the bin (control), (c) the bin (rimed snow), and (d) the bulk model during the same period as Fig. 3.

is assumed to be 3 dB, and the value from the radar to the target A_g is formulated in the following form:

$$A_g = 3 \times (1 - e^{-z/H})(\text{dB}) \text{ (shipborne radar)}, \quad (6)$$

$$A_g = 3 \times e^{-z/H}(\text{dB}) \text{ (spaceborne radar)}, \quad (7)$$

where $H = 2.735$ km is the scale height estimated from the result in Hogan and Illingworth (1999).

Only in the case of shipborne radar on the *Mirai*, the radar signal is attenuated by water on the transparent cover (radome) of the radar container, which results from stagnant precipitation. This attenuation effect was corrected for the measurement product using the rainfall measurement data on the ship; 9 dB was added uniformly in the all vertical layers when the measured precipitation rate was more than 0.01 mm min^{-1} following Okamoto et al. (2007) (hereinafter, called radome correction).

Doppler velocity v_d, defined as the sum of reflectivity-weighted particle fall velocity and vertical wind velocity, is given in the modified form of Matrosov et al. (1994):

$$v_d = w + \frac{\displaystyle\int_{r_{\min}}^{r_{\max}} dn(r)/dr \cdot C_{bk}(r)v_f(r)\,dr}{\displaystyle\int_{r_{\min}}^{r_{\max}} dn(r)/dr \cdot C_{bk}(r)\,dr}, \qquad (8)$$

where w is the vertical wind velocity and v_f is the terminal fall velocities of the hydrometeor particles. In the bin microphysics case, v_f is given in the following form:

$$v_f(r) = -V_t(r)\sqrt{p_0/p}, \qquad (9)$$

where p is the pressure, p_0 stands for the standard reference pressure set at 1000 hPa, and V_t is the terminal fall velocities of hydrometeor particles at p_0 according to their sizes and types (Khain and Sednev 1995) (Fig. 2a). In the case of the bulk microphysics, v_f is given by the following equation:

$$v_f(r) = -\alpha(0.5r)^\beta(\rho_{a0}/\rho_a)^\gamma, \qquad (10)$$

where α, β, and γ are the constants, which can be found in Eito and Aonashi (2009). The relationship between velocity and size is summarized in Fig. 2b. Similar to the calculation of Ze, Eq. (10) with its built-in PSDs is directly substituted for Eq. (8) after it has been expanded to a spectrum on the size bins.

3. Results

a. Mirai *shipborne Doppler radar (M2223)*

Figure 3 illustrates the time–height cross sections (THCSs) of dBZe, as measured by the 95 GHz radar and calculated through the radar simulator with both the bin and bulk JMA-NHM NWP simulations for the 24-h period from 1200 UTC 22 May to 1200 UTC 23 May 2001. The first half of 22 May is not included in the analysis because few clouds were present during that period, and the second half of 23 May is also not included because of the heavy precipitation. The ice and water hydrometeor layers were partitioned at a height of approximately 4 km. The freezing level was estimated from the temperature profile in the mesoanalysis dataset and the LDR profile measured by the shipborne radar. The upper ice clouds, the lower shallow water clouds, and precipitation from the ice clouds were continuously observed. This overall comparison shows some spatial or temporal mismatches between the measurement and simulation because the data are sampled only on the particular spot. The total prediction error including the
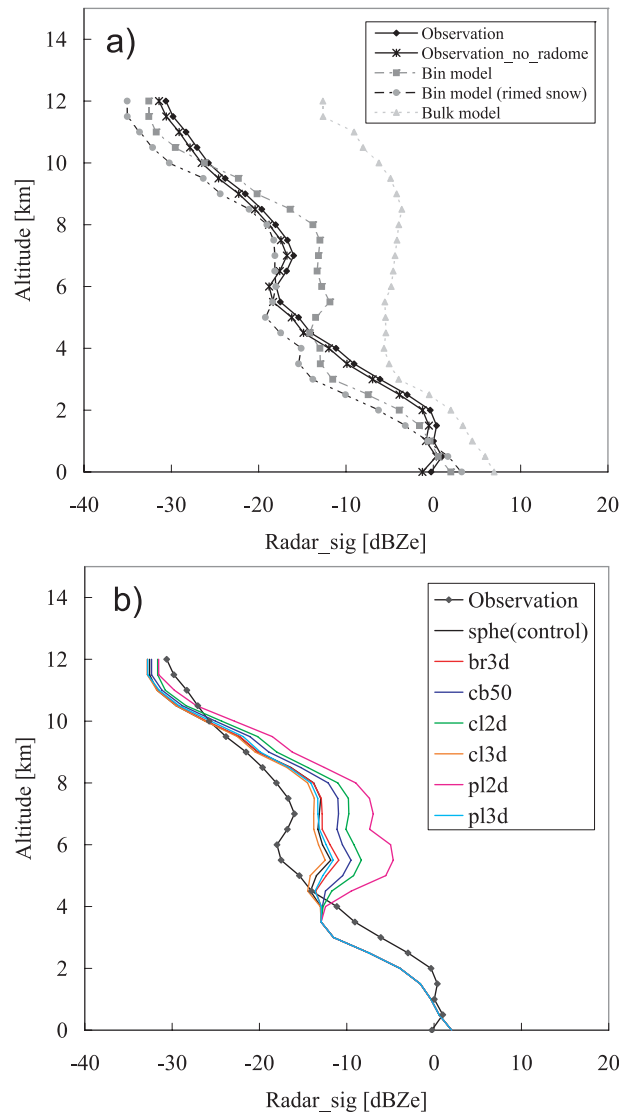

FIG. 5. Vertical distribution of time-averaged dBZe with sampling of the range from −40 to 20 dB. Solid, dash-dotted, dash-double dotted, and dotted lines denote distributions by the radar measurement, the bin (control and rimed snow) simulations, and the bulk model simulation, respectively. (b) Black (sphe; control), red (br3d), blue (cb50), green (cl2d), orange (cl3d), purple (pl2d), and sky blue (pl3d) correspond to distributions using the following models: spherical, bullet-rosette oriented in three-dimensional space (3D bullet-rosette), 50/50 mix of 2D column and 3D bullet-rosette model, hexagonal column oriented in horizontal plane (2D column), hexagonal column oriented randomly in three-dimensional plane (3D column), and hexagonal plate with 2D orientation (2D plate) and random 3D orientation (3D plate) in the DDA computation for backscattering cross sections.

spatial and temporal mismatches should be evaluated in the comparison. However, the mismatches are often under the control of the dataset to make initial and boundary conditions in the NWP simulations rather than the
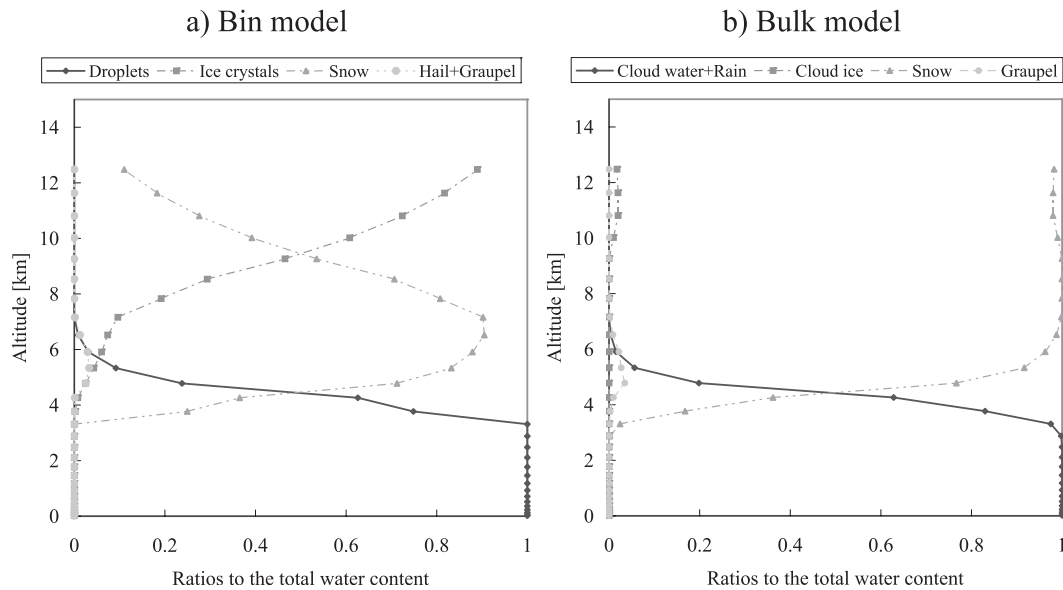
FIG. 6. Vertical distribution of time-averaged mass ratios of each hydrometeor category to the total water contents during the same period as Fig. 3. (a) Droplets (solid line), the total of three types of ice crystals (dash-dotted), snow (dotted), and the total of graupel and hail (dash-double dotted) in the bin model simulation; (b) the total of cloud water and rain (solid line), cloud ice (dash-dotted), snow (dotted), and graupel (dash-double dotted) in the bulk model simulation.

capability of the model physics. To evaluate the performance of the model cloud microphysics, relaxation of the error is attempted by obtaining a temporal average of the result. A quantitative comparison is shown in the forms of the normalized dBZe–height histogram (Fig. 4) and the line chart describing the vertical profiles of the 24-h-averaged dBZe that sampled the range from −40 to 20 dB (Fig. 5a). The radome correction for the dBZe measurement contributes +0.8 dB to the 24-h-averaged dBZe.

Under the freezing level of approximately 4 km, the Ze profiles of the simulations share some common characteristics with that of the observed data. The high-frequency dBZe bands in the observed data and the bin and bulk simulations converge from approximately −10 to +10 dB near the surface in the histograms, and the averaged dBZe shifts to a lower value with altitude. The underestimations of dBZe in the bin model simulations are seen from 2 to 4 km, with an approximately 5-dB difference on average (Fig. 5a). This difference is considered to be due to a partial insufficiency of precipitation from the ice clouds, which is originally caused by a prediction error in the height of ice clouds from 1200 to 2000 UTC 22 May (Fig. 3). In contrast, overestimations of dBZe are highlighted in the ice cloud layers over 4 km in the bin and bulk model simulations. The maximum differences in the 24-h-averaged dBZe are approximately 5 dB near the height of 5 km for the bin model simulation and more than 12 dB for the bulk

model simulation. This overestimation of dBZe is canceled in the bin model simulation considering the fall velocity correction of snow (Figs. 3c, 4c, and 5a). An increase in fall velocities led to a decrease in dBZe through the decrease in both ice water content (IWC) and the mean particle size, because large-size ice hydrometeors were removed more quickly from the layer.

Figure 5b shows the sensitivity of the 24-h-averaged dBZe to different ice particle models in the calculation of the backscattering cross section. The following six nonspherical particle models were also chosen as 3D particle models in the DDA computation: a bullet-rosette oriented in three-dimensional space (3D bullet-rosette), a hexagonal column oriented in a horizontal plane (2D column), a hexagonal column oriented randomly in a three-dimensional plane (3D column), a hexagonal plate with a 2D orientation (2D plate) and random 3D orientation (3D plate), and a 50/50 mix of the 2D column and the 3D bullet-rosette model (CB50). The details of the particle models are given by Sato and Okamoto (2006). The backscattering cross sections of the fractal-shaped snowflakes at 95 GHz are estimated to be best fitted with those of the 2D column model among the spherical and the six nonspherical models (Ishimoto 2008; Okamoto et al. 2010). Figure 5b shows that the difference in dBZe is roughly within the maximum range from −1 to +7 dB, and the difference between the spherical model and the 2D column (considered compatible with fractal snow)
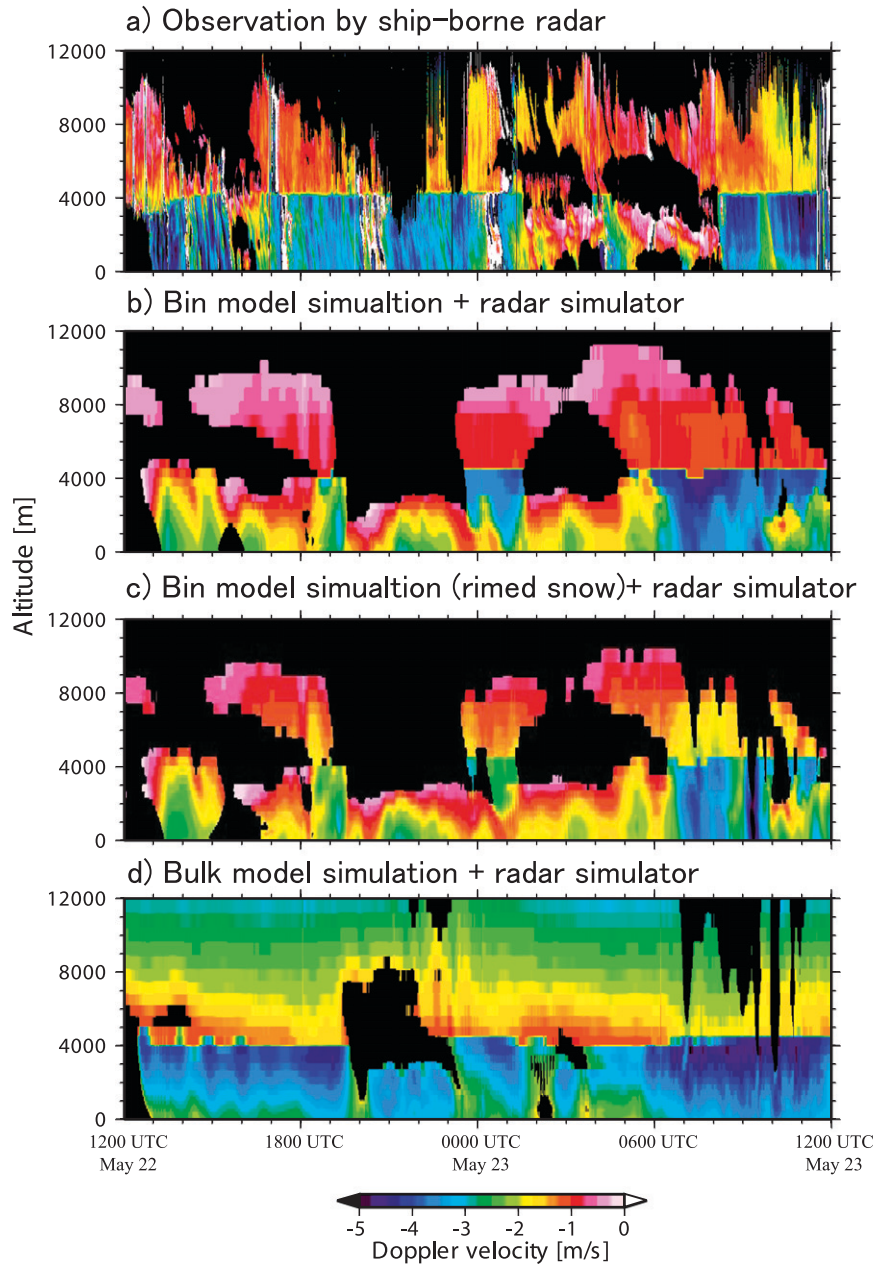
FIG. 7. THCSs of the DVs (a) measured by the 95-GHz *Mirai* Doppler radar, and calculated from the radar product simulator applied to the outputs of (b) the bin (control), (c) the bin (rimed snow), and (d) the bulk model simulations from 1200 UTC 22 May to 1200 UTC 23 May 2001.

model cases is at most 4 dB; the differences depend on the particle size and IWC so that the value shifts smaller with altitude. This result demonstrates that the utilization of the spherical particle model is not a source of the dBZe overestimation in the ice cloud layer.

Figure 6 shows the vertical distribution of the dominant hydrometeor types in both the bin and bulk simulations. These profiles indicate the comparative characteristics of both microphysics and the hydrometer types that caused

the discrepancies between the observed data and the simulations. The overdominance of snow up to the cloud top in the bulk model simulation is consistent with other results using a similar microphysical framework (Hashimoto et al. 2007; Eito and Aonashi 2009). The contoured area of the high frequency in the dBZe–height histogram of the bulk model simulation over 4 km is small in spread (Fig. 4d), and a weak relationship between height and dBZe is seen compared with those of both the observed
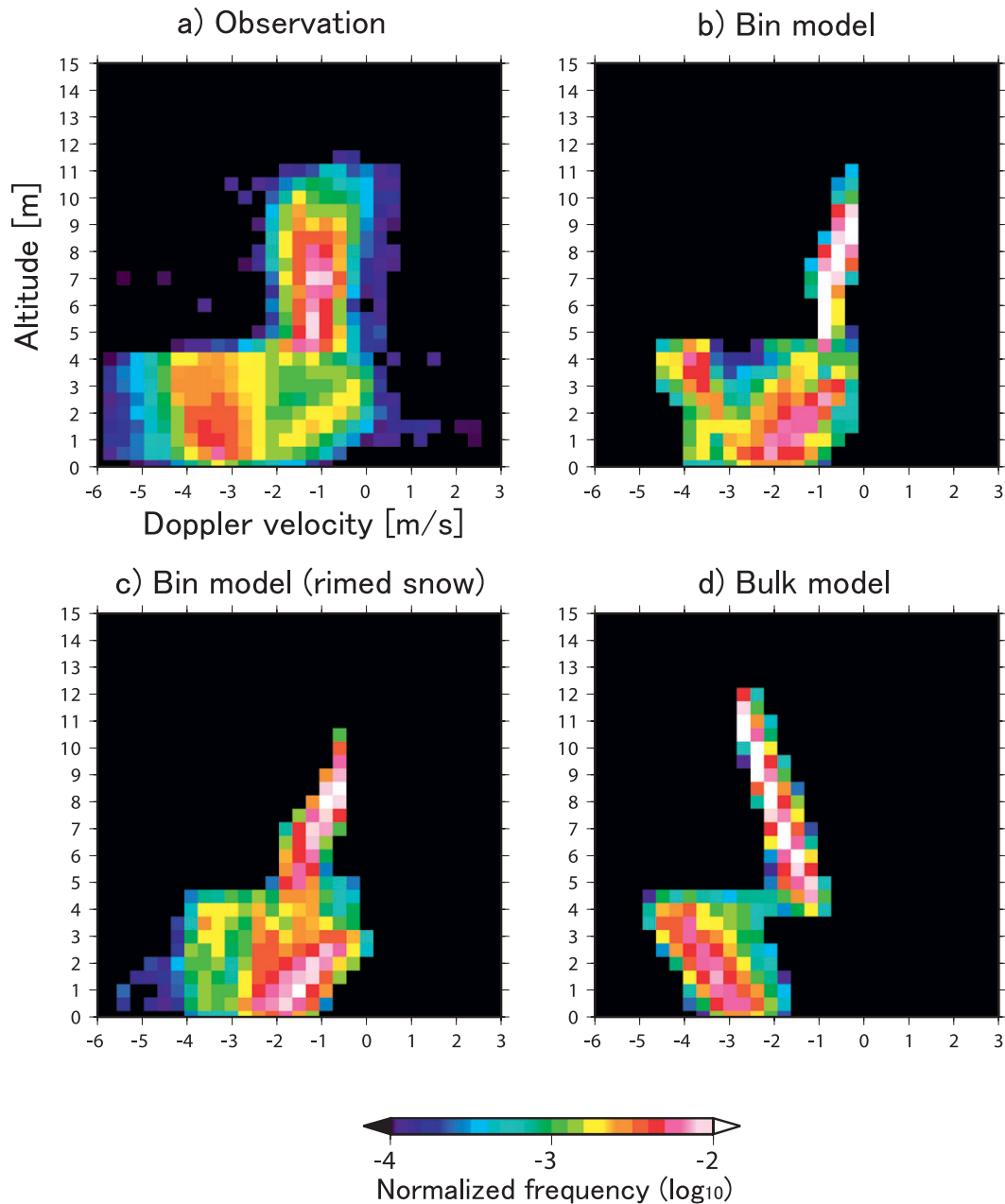
FIG. 8. Normalized DV–height histograms constructed from (a) the radar measurement, (b) the bin (control), (c) the bin (rimed snow), and (d) the bulk model simulation.

data and the bin model simulation. Bodas-Salcedo et al. (2008) indicated that this lack of spread is due to an application of the bulk scheme with an assumption of built-in PSD to the simulator. In contrast, the corresponding spread is sufficiently wide in the histogram of the bin model simulation, suggesting that the direct utilization of prognostic PSD and the distribution of dominant hydrometeor categories may result in a better dBZe simulation. The weak dBZe–height relationship in the bulk model

simulation is caused by using the constant intercept parameter for snow without modeling the dependence on temperature, which can be seen from the comparison with the results in Bodas-Salcedo et al. (2008). In addition, this monotonic Ze structure in the bulk model simulation may likely be attributable to the remarkable predominance of snow over cloud ice (Fig. 6b).

An analysis of DV offers an additional perspective to evaluate the differences between the observed data and
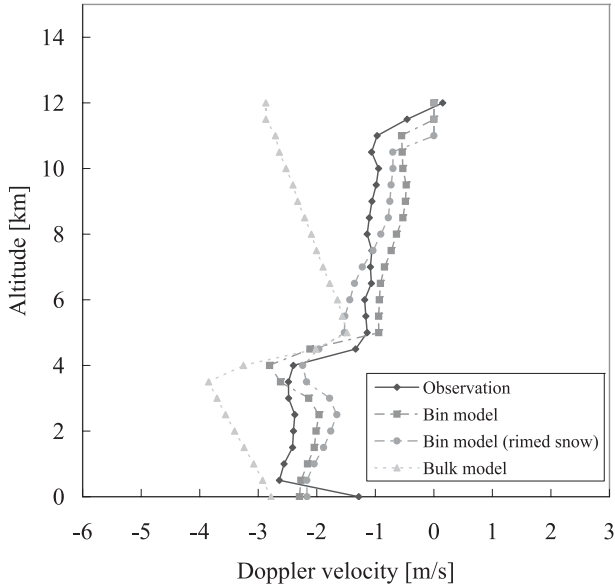
FIG. 9. Vertical distribution of the time-averaged Doppler velocity by radar measurement (solid), bin simulation (control) (dash-dotted), bin simulation (rimed snow) (dash-double dotted), and bulk model simulation (dotted).
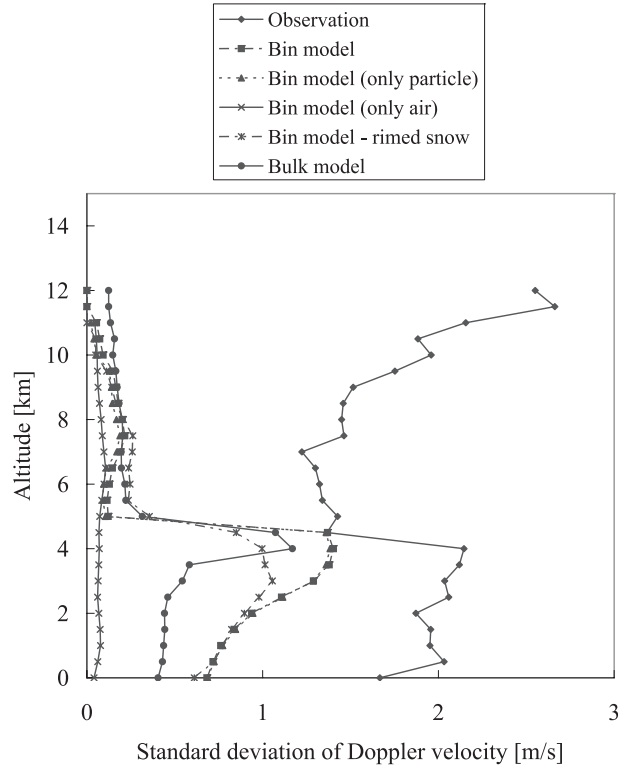

FIG. 10. Vertical distribution of the standard deviations of Doppler velocity from the time average by radar measurement (diamonds), in the bin simulation (control) (squares), only from the terminal fall velocities of hydrometeor particles in the bin simulation (triangles), from vertical wind velocity in the bin model simulation (control) (crosses), bin simulation (rimed snow) (asterisks), and bulk model simulation (circles).

the simulations (Figs. 7, 8, and 9). Note that the negative velocities are downward, and the radar-observed and simulated DVs are shown only on vertical areas of the dBZe larger than −20 dB. The characteristics of vertical structures are separated between the water and ice cloud layers, similarly to those of Ze. The DV–height histograms of the observation and the bin model simulations share some common characteristics: a unimodal distribution is dominant over the freezing level of roughly 4 km aloft, while a bimodal distribution is seen under the level. The small DV mode at approximately −3.5 m s^{-1} in the bimodal distribution corresponds to the precipitation from ice clouds over the freezing level, whereas the large DV mode at approximately −1 m s^{-1} corresponds to warm clouds whose cloud tops do not reach the freezing level. The very weak dominance of the small DV mode in the bin model simulation most likely indicates a partial insufficiency of precipitation from the ice clouds, as in the dBZe comparison.

The bulk model simulation clearly underestimated the DV. The velocity decreases with altitude in the water and ice cloud layers individually because the low air density in the upper atmosphere results in an increase in the particle fall velocity [Eq. (10)]. The small particle classes such as cloud water and cloud ice, whose fall velocity is nearly zero, has little contribution to forming DV, probably because these classes are less dominant and the monodispersive PSDs with small particle sizes cause very small reflectivity. The vertically constant DV

in the bin model simulations suggests that the decrease of DV with altitude should be offset by a decrease in the fall velocity through a decrease in particle size in the cloud microphysics. However, this effect does not work properly in the bulk model simulation.

Even the bin model simulation cannot reproduce the observed wide spread over 4 km in the DV–height histogram. A poor reproducibility of the vertical wind velocity to DV in the simulation could be a source of the discrepancy, although the velocity averaged over a long period at a given altitude would be expected to converge to almost zero in uniform stratiform cloud cases (Orr and Kropfli 1999). Figure 10 shows vertical profiles of the standard deviation of DV from their averaged values in the observation and the simulations. A characteristic common to all profiles is a jump at approximately 5 km (i.e., the boundary between the ice and water cloud layers). This jump is considered to be due to a difference in the dependence of the terminal fall velocity on particle size between liquid-phase and ice-phase particles (Fig. 2).

Under 4km

a) Observation

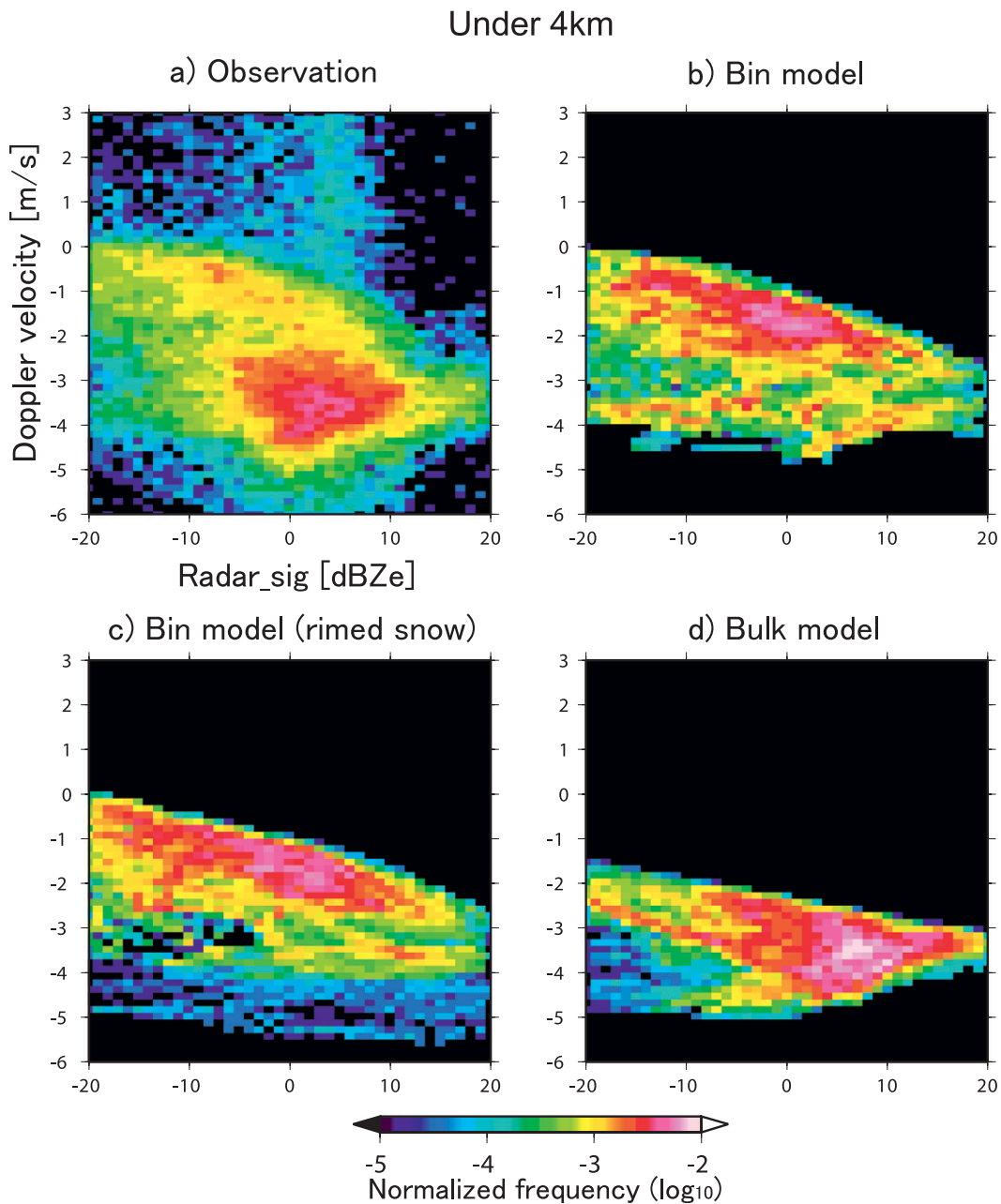b) Bin model

c) Bin model (rimed snow)

d) Bulk model

FIG. 11. Normalized dBZe–DV histograms under heights of 4 km constructed from (a) the radar measurement, (b) the bin (control), (c) the bin (rimed snow), and (d) the bulk model simulation.

There is a somewhat constant difference between the profiles of the observation and simulations regardless of altitude, except over 10 km. This difference could be related to the difference of the spatial dispersion of the vertical wind velocity between the real atmosphere and the model simulations. Although an accurate value of the standard deviation contributed by the real wind velocity cannot be calculated in this analysis, a value on the order of 0.1 m s^{-1} is feasible compared with the retrieval result of the measurement using the same radar for tropical cirrus clouds (Sato et al. 2009). In contrast, both the standard deviation and the average (not figured) of the vertical wind velocity in the model simulations are approximately less than 0.1 m s^{-1} at any altitude. The difference is probably due to the coarse horizontal and vertical resolution of the present NWP simulation. We speculate that a horizontal resolution on the order of 10 or 1 m is required to reproduce a realistic
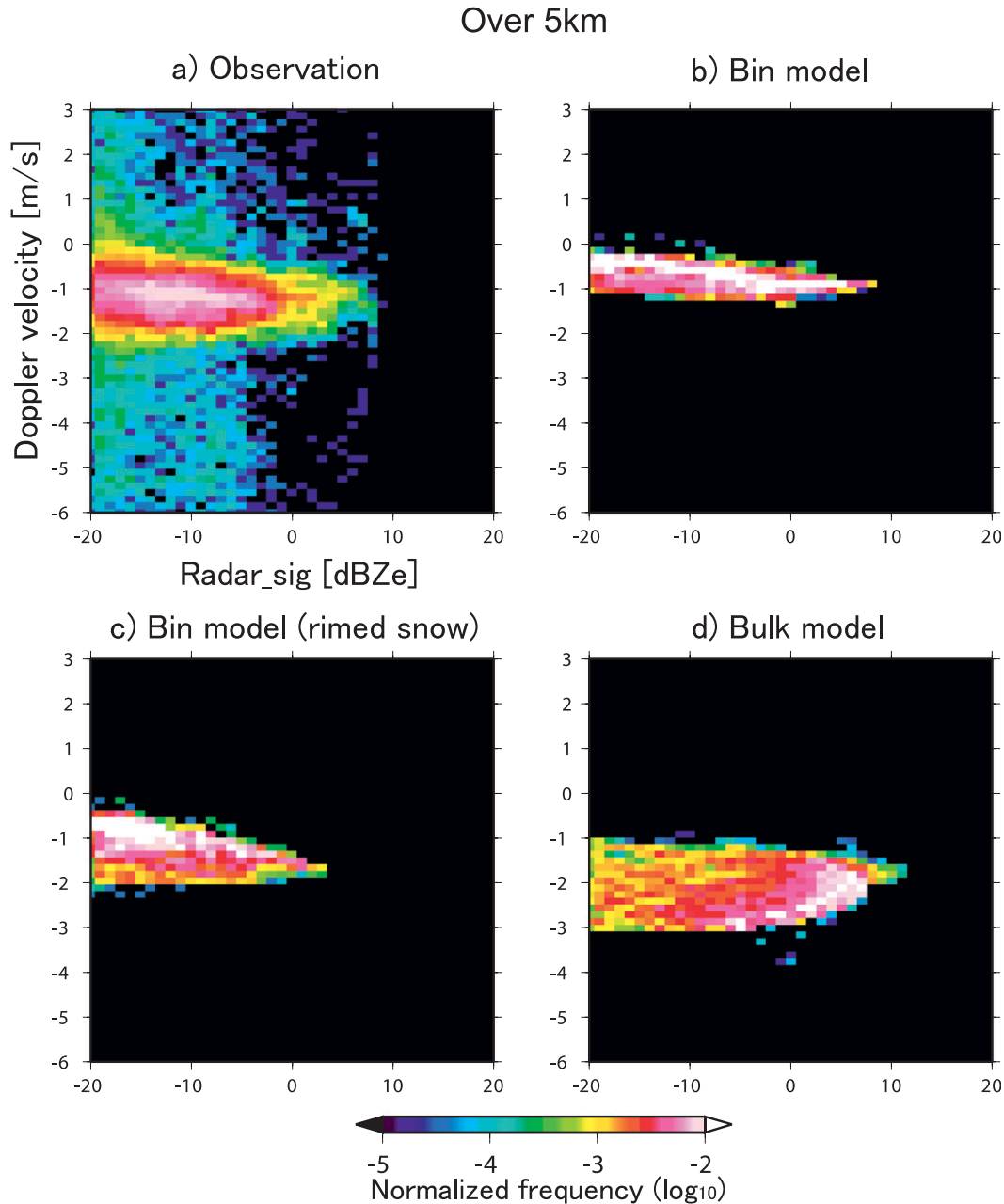
Over 5km

FIG. 12. As in Fig. 11, but over heights of 5 km.

dispersion of the vertical wind velocity on a grid-scale simulation. Khairoutdinov and Randall (2003) showed the sensitivity of vertical velocity variance to the horizontal resolution in the 28-day simulation during summer over Southern Great Plains area. The magnitude of variance in the 250-m resolution run is approximately twice as much as that in the 2-km run. Although the conditions of their simulation are largely different from ours, much higher horizontal resolution than 250 m is possibly required to improve our result.

The dBZe–DV correlations are principal aspects representative of cloud microphysics for the Doppler radar measurement and simulation. The variables are influenced by certain relevant physical factors, as in Eqs. (1) and (8). Figures 11, 12, and 13 show the dBZe–DV relationships in the form of histograms and line graphs of the averaged DV with respect to the dBZe range of 1 dB. The observations and simulations share a common characteristic: the DV decreases (negative velocities are downward) with dBZe under a height of 4 km, whereas the DV
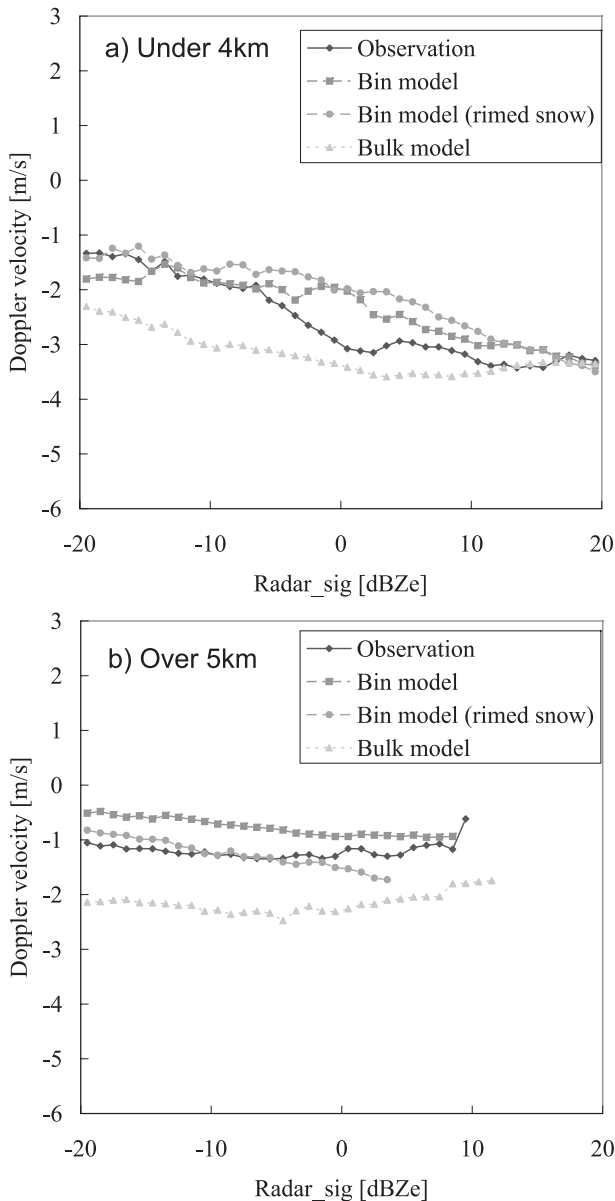
FIG. 13. dBZe-averaged DV (a) under heights of 4 km and (b) over heights of 5 km. Solid, dash-dotted, dash-double dotted, and dotted lines denote distributions by the radar measurement, the bin (control and rimed snow) simulations, and the bulk model simulation, respectively.

is nearly constant with respect to dBZe over 5 km. This feature is considered to be due to the differences of the uniformity of particle size and the dependence of the particle fall velocity on particle size between the ice-phase and liquid-phase clouds. A unimodal distribution in the histograms is observed over 5 km (Fig. 12). The bin model with snow fall velocity correction is the best simulation with respect to the occurrence and the averaged DV (Fig. 13b). Under 4 km, a rough bimodal distribution centered

at approximately (-5 dB, -1 m s^{-1}) and (5 dB, -2.5 m s^{-1}) is noticed in the histogram plot of the observed data (Fig. 11). This distribution is organized by large raindrops included in the precipitation from the ice clouds and relatively small cloud droplets in the shallow water clouds. In contrast, the histograms of the simulations highlight only approximately one mode, as observed in the comparison of the DV vertical histograms (Fig. 8). In Fig. 11, the profiles of the two bin model simulations show only the mode near (-5 dB, -1 m s^{-1}) in the observed profile; this result indicates a partial insufficiency of precipitation from the ice clouds also. The bulk simulation profile shows only another mode near (5 dB, -2.5 m s^{-1}); the mode by shallow water clouds cannot be reproduced probably because of slight dominance of the cloud water class in the bulk model simulation.

b. CloudSat spaceborne CPR (C2873 and C2917)

Comparing the simulations for the models and the *CloudSat* CPR observations may introduce another viewpoint to the issue. Ice clouds can be measured without attenuations by gas and hydrometeors under the target, which subsequently has a large influence on the calculation of the Ze of the ice clouds in the case of the shipborne observation. The dBZe profiles were illustrated for C2873 and C2917 in the form of the latitude–height cross sections (LHCSs) (Figs. 14 and 15, respectively). The freezing level was approximately located at a height of 1–2 km in both cases. Figure 16 shows line charts for the vertical profile of the horizontally averaged dBZe with sampling from -40 to 20 dB. The overestimations of dBZe in the ice cloud layers are highlighted, as in the case of M2223.

For C2873, significant overestimations of PIA due to hydrometeors are highlighted, especially over the latitude from 40° to 44°N (Fig. 17). Ice clouds are a considerable cause of the overestimations because the simulated PIA from the top to a height of 2.5 km already exceeds the total PIA of the *CloudSat* product (not figured). The result demonstrates that the overestimations of dBZe and the attenuation are due to the characteristics of the simulated ice clouds themselves. Figures 14b and 14d show that part of Ze is less than -40 dB in the lower layer under 2 km. This feature is also attributed to strong attenuation in the ice clouds, although precipitation was actually simulated there. The adjustment in the additional run of the bin microphysics with the rimed snow is able to reduce the overestimations of PIA and Ze, leading to agreement with the observed data (Figs. 14c and 16a) because the vertical distribution of the dominant hydrometeor types (Fig. 18a) is similar to that in the M2223 case (Fig. 6a): Snow and ice crystals are dominant in the ice clouds of the bin model simulation, whereas only snow is dominant in the bulk model simulation.
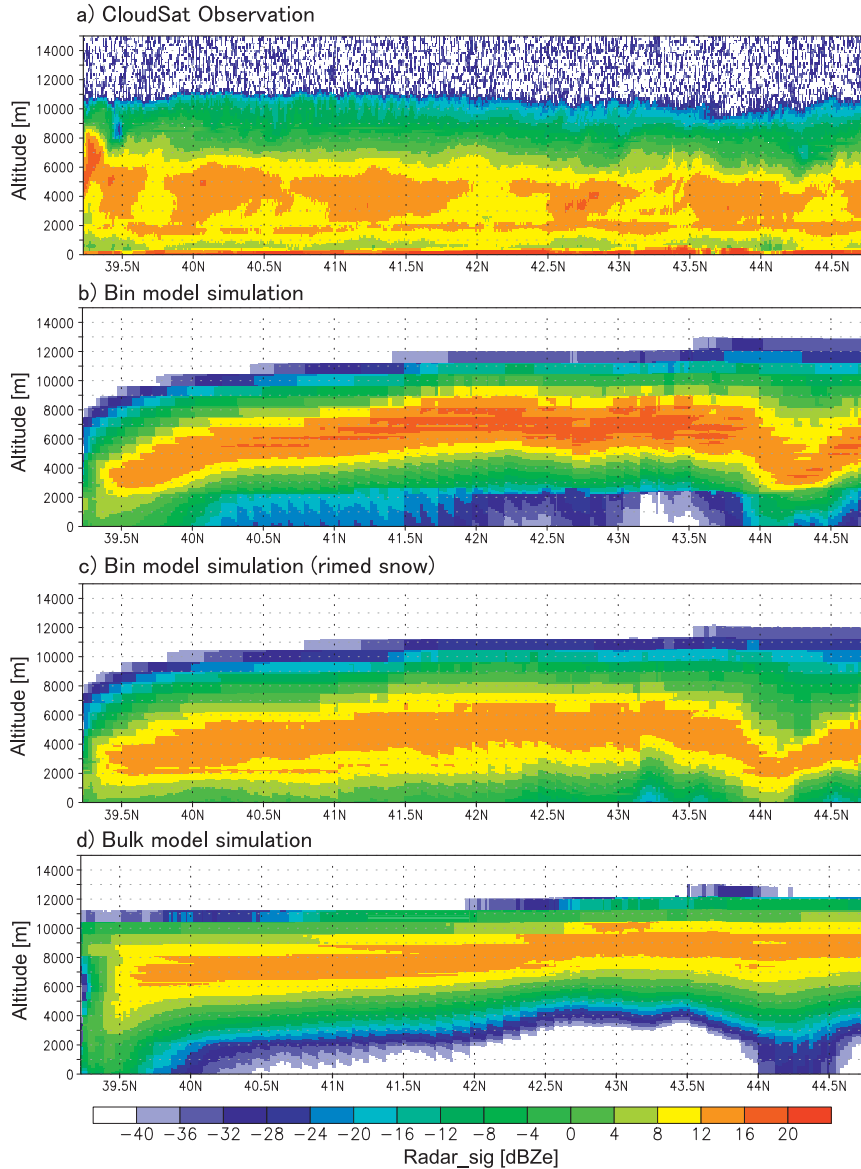
FIG. 14. Latitude–height cross sections of equivalent radar reflectivity factors in the case of nimbostratus on 11 Nov 2006 (a) measured by the *CloudSat* CPR, and calculated using the radar simulator applied to the outputs of (b) the bin (control), (c) the bin (rimed snow), and (d) the bulk model simulation.

In the case of C2917, shallow convective clouds, including more supercooled water, were simulated. Consequently, hail and graupel were present in relatively high percentages compared with the other cases in both simulations (Figs. 18c,d). As a result, the adjustment of the bin microphysics with the riming did not significantly improve the discrepancy between the observed data and the simulation (Fig. 16b) because these modulations are mostly effective in changing the microphysical structures of snow and ice crystals. In addition, an error in the simulations of the macrophysical structures of clouds

may cause the overestimation in this case. The cloud-top heights were simulated to be over 4 km in the northern part of the latitude from 38.5°N, which is not in agreement with the observed data. The result suggests stronger convection, which causes increases in IWC, mean particle size, and, subsequently, dBZe.

4. Conclusions

In this paper, we conducted NWP simulations using JMA-NHM with bin and bulk microphysics for three
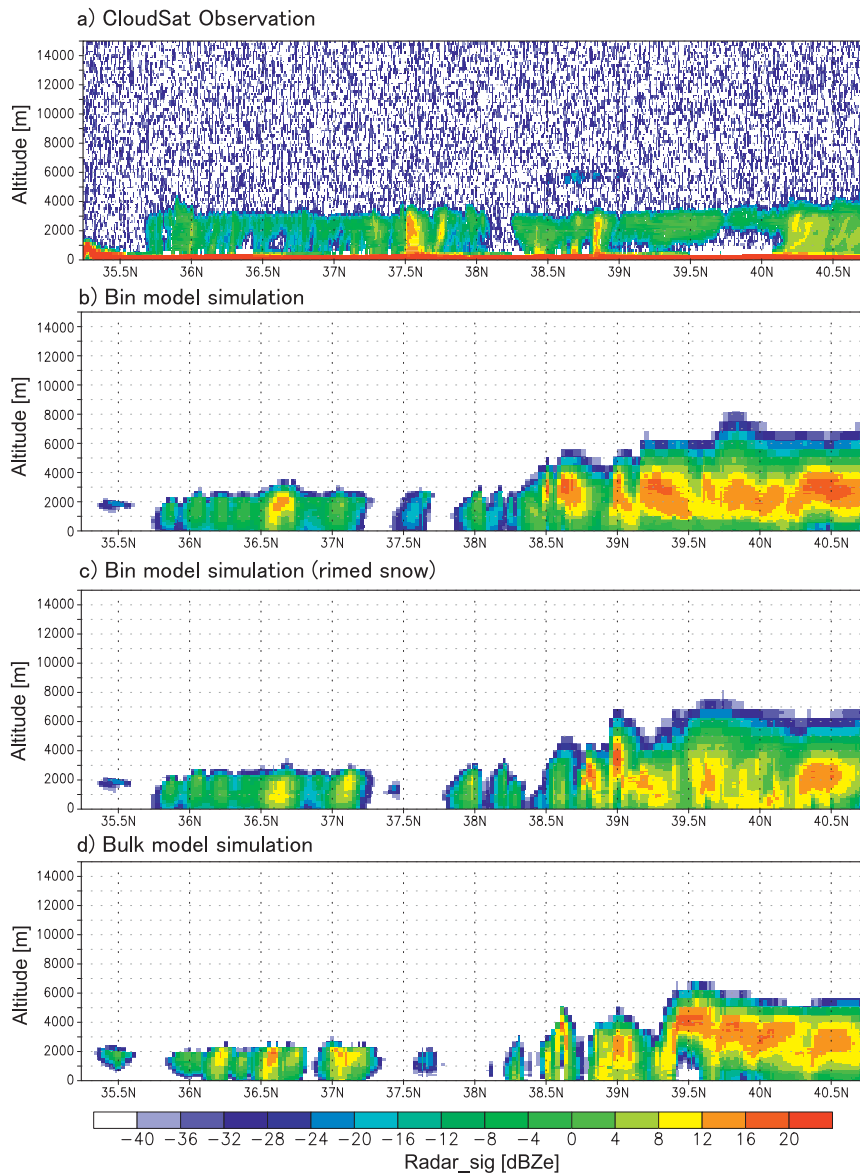
FIG. 15. As in Fig. 14, but for the case of convective clouds on 14 Nov 2006.

cases to be compared with shipborne or spaceborne cloud radar observations. Direct comparisons were performed with a radar product simulator applied to the output of the NWP simulations. The results documented some important characteristics and problems of microphysics simulation in the bin and bulk models. The bin model can generally provide better Ze and DV simulations than the bulk model. The modification of the terminal fall velocities of snowflakes equalized to those of hail in all size bins is considerably effective for improving the result. The result suggests that there is something wrong in the mass–size and size–terminal fall velocity relations of snowflakes in the present bin microphysics.

The consequence is consistent with the result of the study using the same bin microphysics core (Fan et al. 2009). Insufficient modeling of the riming process is a possible source of the problem, although a significant amount of supercooled water is not predicted in the simulation. Advanced microphysical models explicitly calculating a rimed fraction of snow have the potential to provide a better simulation. A poor modeling of snow aggregation is one of the possibilities but the required increase in fall velocity is considered not to be achieved using a different shape assumption of snow aggregates without riming (Pruppacher and Klett 1997). Another possibility is an underestimation of increase in the terminal fall
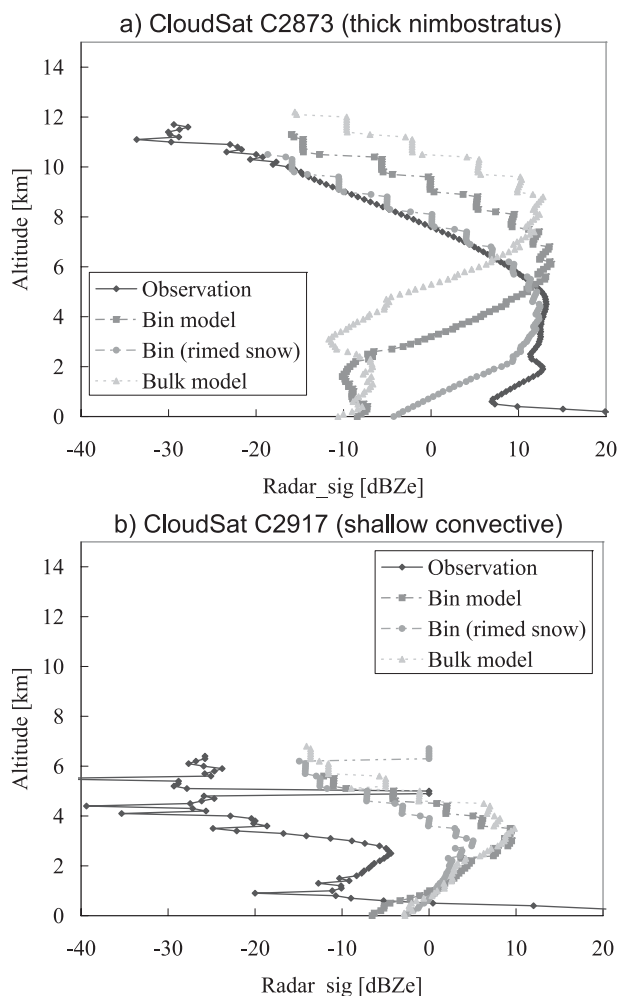
FIG. 16. Vertical distributions of the horizontally averaged dBZe sampling the range from −40 to 20 dB in (a) Fig. 14 and (b) Fig.15.

FIG. 17. Horizontal distributions of the path integration attenuation (PIA) in the case of nimbostratus on 11 Nov 2006.

velocity aloft by decrease in air pressure or density. In Lin et al. (1983), the square root factor in the equation is derived from the study of Foote and du Toit (1969) about the terminal velocity of raindrops aloft. It is uncertain whether the exponents of the factor for liquid-phase and ice-phase particles are the same, since their drag coefficients are different. In addition, there still remains a lack of understanding how temporal or spatial mismatches between measurement and simulation affect the result of comparison, although the effect can be relaxed in a quantitative analysis. An insufficiency of precipitation from ice clouds is observed in the one case, and the problem should be investigated in sampling many cases in future work.

We provide some suggestions for improving the bulk microphysics that are based upon comparisons with the observed data and the bin model result. First, one of the problems in Ze simulation with the bulk microphysics is
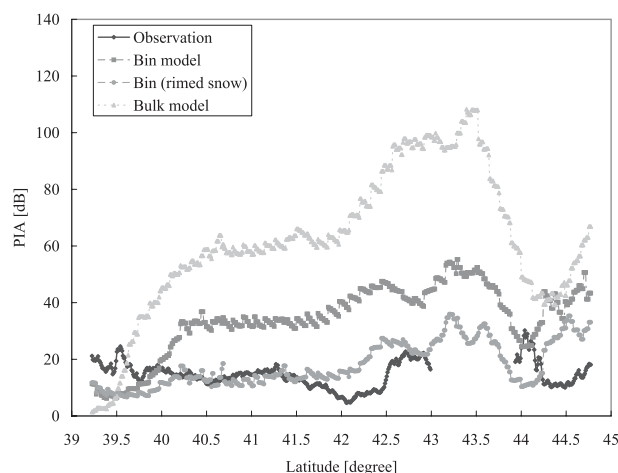
a lack of countered spread in the histogram for ice clouds. Bodas-Salcedo et al. (2008) suggested that it is necessary to predict the number concentration in a double-moment framework. However, at least in our cases, a lack of dBZe spread of ice clouds may be resolved if different classes coexist adequately because snow is overdominant in the bulk model simulation compared with the bin model result. The overdominance of snow is considered to be due to the large depositional growth to snow (Eito and Aonashi 2009). Second, the vertical structure of the DV in the bulk model simulation is clearly different from those of the observed data and the bin model simulation. The fall velocity in each cloud class is dependent on the mixing ratio and air density. A decrease in DV with altitude due to changes in air density should be offset by increases due to changes in particle size; however, the increases do not function in the bulk model simulation. The effect should be introduced in the calculation of the fall velocity, even in single-moment bulk microphysics. A double-moment bulk microphysics can calculate the fall velocity by taking into account changes in the mean particle size, and hence the problem is also avoidable.

An additional approach using multiwavelength remote sensing is useful for further study. Lidar observations are often accompanied by W-band radar observations, such as *CALIPSO* with *CloudSat*. A spaceborne lidar is ideal for detecting thin cirrus; a fraction of up to 70% of upper clouds detected by *CloudSat* can be measured by the lidar. Measuring very thick clouds using the lidar is difficult because they cannot be penetrated by the lasers. In such regions, the combination of X-band, C-band, or Ka-band radar with W-band could offer a potential solution. X-band, C-band, or K-band frequencies are
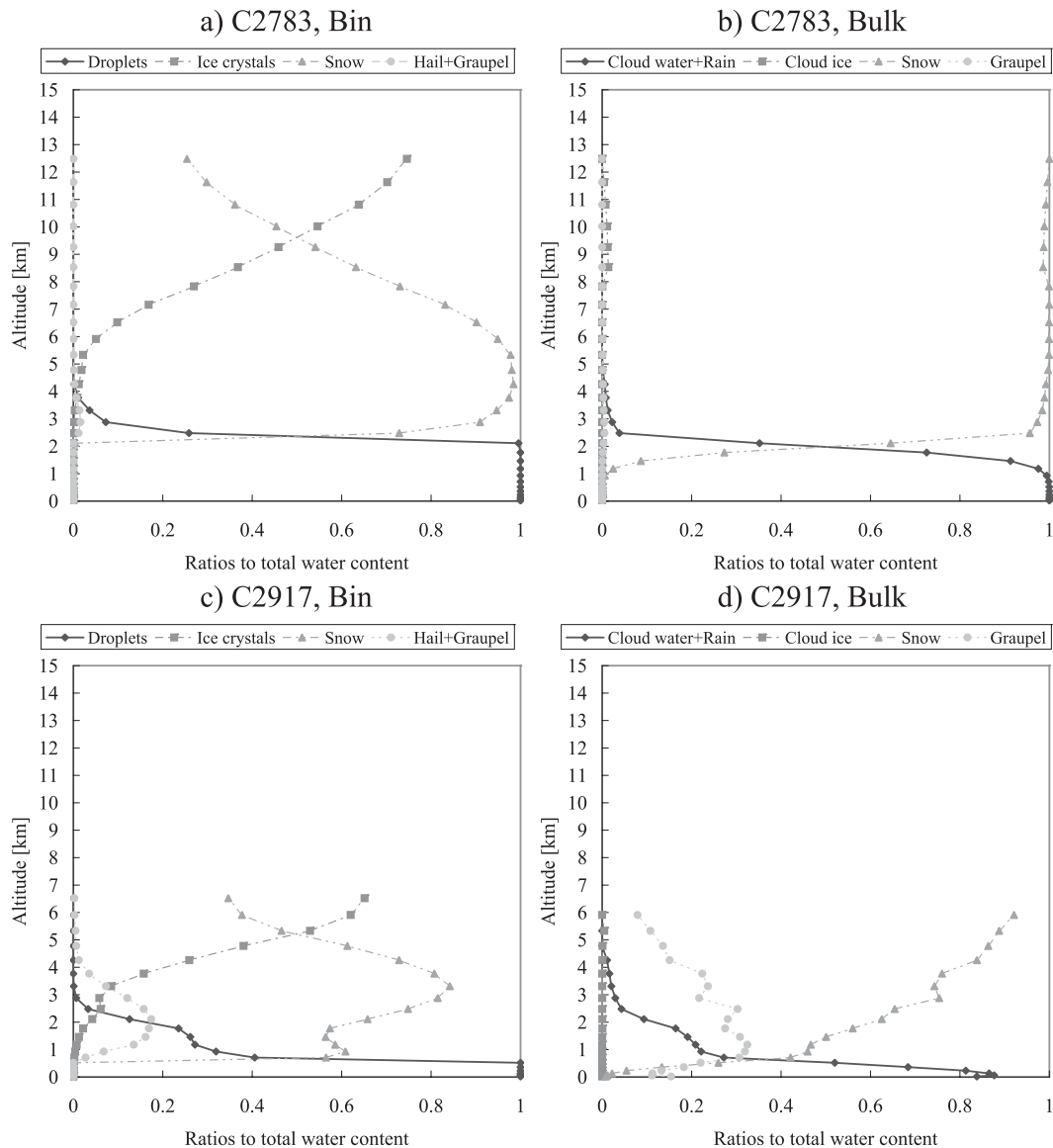
FIG. 18. Vertical distribution of the horizontally averaged mass ratios of each hydrometeor category to the total water contents in the *CloudSat* cases. (a),(c) Droplets (solid line), the total of three types of ice crystals (dash-dotted), snow (dotted), and the total of graupel and hail (dash-double dotted) in the bin simulation; (b),(d) the total of cloud water and rain (solid line), cloud ice (dash-dotted), snow (dotted), and graupel (dash-double dotted) in the bulk model simulation.

sometimes used together with the W-band frequency; TRMM PR and *CloudSat* for global data constitute an example (Masunaga et al. 2008). K-band multiwavelength radars or radiometers are utilized to observe clouds on site (e.g., Illingworth et al. 2007) and are currently being prepared in the Global Precipitation Measurement (GPM) mission as a next-generation satellite-based observation. In addition, collaboration between radar remote sensing and on-site measurement is necessary to verify the microphysics. This kind

of measurement campaign is often performed for the purpose of on-site validation of instruments for remote sensing.

REFERENCES

Bodas-Salcedo, A., M. J. Webb, M. E. Brooks, M. A. Ringer, K. D. William, S. F. Milton, and D. R. Wilson, 2008: Evaluating cloud systems in the Met Office global forecast model using simulated CloudSat radar reflectivities. *J. Geophys. Res.,* **113,** D00A13, doi:10.1029/2007JD009620.

Clothiaux, E., M. Miller, B. Albrecht, T. Ackerman, J. Verlinde, D. Babb, R. Peters, and W. Syrett, 1995: An evaluation of a 94-GHz radar for remote sensing of cloud properties. *J. Atmos. Oceanic Technol.,* **12,** 201–229.

Cotton, W. R., G. J. Tripoli, R. M. Rauber, and E. A. Mulvihill, 1986: Numerical simulation of the effects of varying ice crystal nucleation rates and aggregation processes on orographic snowfall. *J. Climate Appl. Meteor.,* **25,** 1658–1680.

Eito, H., and K. Aonashi, 2009: Verification of hydrometeor properties simulated by a cloud-resolving model using a passive microwave satellite and ground-based radar observations for a rainfall system associated with the Baiu front. *J. Meteor. Soc. Japan,* **87A,** 425–446, doi:10.2151/jmsj.87A.425.

Fan, J., M. Ovtchinnikov, J. M. Comstock, S. A. McFarlane, and A. Khain, 2009: Ice formation in Arctic mixed-phase clouds: Insights from a 3-D cloud-resolving model with size-resolved aerosol and cloud microphysics. *J. Geophys. Res.,* **114,** D04205, doi:10.1029/2008JD010782.

Foote, G. B., and P. S. du Toit, 1969: Terminal velocity of raindrops aloft. *J. Appl. Meteor.,* **8,** 249–253.

Hashimoto, A., M. Murakami, T. Kato, and M. Nakamura, 2007: Evaluation of the influence of saturation adjustment with respect to ice on meso-scale model simulations for the case of 22 June, 2002. *SOLA,* **3,** 85–88, doi:10.2151/sola.2007-022.

Hasumi, H., and S. Emori, Eds., 2004: K-1 coupled model (MIROC) description. K-1 Tech. Rep. 1, Center for Climate System Research, University of Tokyo, 34 pp.

Haynes, J. M., R. T. Marchand, Z. Luo, A. Bodas-Salcedo, and G. L. Stephens, 2007: A multipurpose radar simulation package: QuickBeam. *Bull. Amer. Meteor. Soc.,* **88,** 1723–1727.

——, T. S. L'Ecuyer, G. L. Stephens, S. D. Miller, C. Mitrescu, N. B. Wood, and S. Tanelli, 2009: Rainfall retrieval over the ocean with spaceborne W-band radar. *J. Geophys. Res.,* **114,** D00A22, doi:10.1029/2008JD009973.

Hogan, R. J., and A. J. Illingworth, 1999: The potential of spaceborne dual-wavelength radar to make global measurements of cirrus clouds. *J. Atmos. Oceanic Technol.,* **16,** 518–531.

Horie, H., T. Iguchi, H. Hanado, H. Kuroiwa, H. Okamoto, and H. Kumagai, 2000: Development of a 95-GHz airborne cloud profiling radar (SPIDER): Technical aspects. *IEICE Trans. Commun.,* **E83-B,** 2010–2020.

Iguchi, T., T. Nakajima, A. P. Khain, K. Saito, T. Takemura, and K. Suzuki, 2008: Modeling the influence of aerosols on cloud microphysical properties in the East Asia region using a mesoscale model coupled with a bin-based cloud microphysics scheme. *J. Geophys. Res.,* **113,** D14215, doi:10.1029/2007JD009774.

Ikawa, M., and K. Saito, 1991: Description of a non-hydrostatic model developed at the Forecast Research Department of the MRI. MRI Tech. Rep. 28, 238 pp. [Available online at http://www.mri-jma.go.jp/Publish/Technical/DATA/VOL_28/28_en.html.]

Illingworth, A. J., and Coauthors, 2007: Cloudnet: Continuous evaluation of cloud profiles in seven operational models using ground-based observations. *Bull. Amer. Meteor. Soc.,* **88,** 883–898.

Inoue, T., M. Satoh, Y. Hagihara, H. Miura, and J. Schmetz, 2010: Comparison of high-level clouds represented in a global cloud-system resolving model with CALIPSO/CloudSat and geostationary satellite observations. *J. Geophys. Res.,* **115,** D00H22, doi:10.1029/2009JD012371.

Ishimoto, H., 2008: Radar backscattering computations for fractal-shaped snowflakes. *J. Meteor. Soc. Japan,* **86,** 459–469.

Khain, A. P., and I. L. Sednev, 1995: Simulation of hydrometeor size spectra evolution by water–water, ice–water and ice–ice interactions. *Atmos. Res.,* **36,** 107–138, doi:10.1016/0169-8095(94)00030-H.

——, M. Ovtchinnikov, M. Pinsky, A. Plkrovsky, and H. Krugliak, 2000: Notes on the state-of-the-art numerical modeling of cloud microphysics. *Atmos. Res.,* **55,** 159–224, doi:10.1016/S0169-8095(00)00064-8.

——, A. Pokrovsky, D. Rosenfeld, U. Blahak, and A. Ryzhkov, 2011: The role of CCN in precipitation and hail in a mid-latitude storm as seen in simulations using a spectral (bin) microphysics model in a 2D dynamic frame. *Atmos. Res.,* **99,** 129–146.

Khairoutdinov, M. F., and D. A. Randall, 2003: Cloud resolving modeling of the ARM summer 1997 IOP: Model formulation, results, uncertainties, and sensitivities. *J. Atmos. Sci.,* **60,** 607–625.

Kikuchi, N., T. Nakajima, H. Kumagai, H. Kuroiwa, A. Kamei, R. Nakamura, and T. Y. Nakajima, 2006: Cloud optical thickness and effective particle radius derived from transmitted solar radiation measurements: Comparison with cloud radar observations. *J. Geophys. Res.,* **111,** D07205, doi:10.1029/2005JD006363.

Lhermitte, R., 1987: A 94-GHz Doppler radar for cloud observations. *J. Atmos. Oceanic Technol.,* **4,** 36–48.

Li, X., W.-K. Tao, T. Matsui, C. Liu, and H. Masunaga, 2010: Improving a spectral bin microphysics scheme using TRMM satellite observations. *Quart. J. Roy. Meteor. Soc.,* **136,** 382–399, doi:10.1002/qj.569.

Lin, Y. H., R. D. Farley, and H. D. Orville, 1983: Bulk parameterization of the snow field in a cloud model. *J. Climate Appl. Meteor.,* **22,** 1065–1092.

Mace, G. G., R. Marchand, Q. Zhang, and G. Stephens, 2007: Global hydrometeor occurrence as observed by CloudSat: Initial observations from summer 2006. *Geophys. Res. Lett.,* **34,** L09808, doi:10.1029/2006GL029017.

Marchand, R., G. G. Mace, T. Ackerman, and G. Stephens, 2008: Hydrometeor detection using *CloudSat*—An Earth-orbiting 94-GHz cloud radar. *J. Atmos. Oceanic Technol.*, **25,** 519–533.

——, J. Haynes, G. Mace, T. Ackerman, and G. Stephens, 2009: A comparison of simulated cloud radar output from the multiscale modeling framework global climate model with Cloud-Sat cloud radar observations. *J. Geophys. Res.*, **114,** D00A20, doi:10.1029/2008JD009790.

Masunaga, H., M. Satoh, and H. Miura, 2008: A joint satellite and global cloud-resolving model analysis of a Madden–Julian oscillation event: Model diagnosis. *J. Geophys. Res.*, **113,** D17210, doi:10.1029/2008JD009986.

——, and Coauthors, 2010: Satellite data simulator unit: A multisensor, multispectral satellite simulator package. *Bull. Amer. Meteor. Soc.*, **91,** 1625–1632.

Matrosov, S. Y., B. W. Orr, R. A. Kropfli, and J. B. Snider, 1994: Retrieval of vertical profiles of cirrus cloud microphysical parameters from Doppler radar and infrared radiometer measurements. *J. Appl. Meteor.*, **33,** 617–626.

Miura, H., M. Satoh, T. Nasuno, A. T. Noda, and K. Oouchi, 2007: A Madden–Julian oscillation event realistically simulated by a global cloud-resolving model. *Science,* **318,** 1763–1765, doi:10.1126/science.1148443.

Okamoto, H., 2002: Information content of the 95-GHz cloud radar signals: Theoretical assessment of effects of nonsphericity and error evaluations of the discrete dipole approximation. *J. Geophys. Res.*, **107,** 4628, doi:10.1029/2001JD001386.

——, S. Iwasaki, M. Yasui, H. Horie, H. Kuroiwa, and H. Kumagai, 2003: An algorithm for retrieval of cloud microphysics using 95-GHz cloud radar and lidar. *J. Geophys. Res.*, **108,** 4226, doi:10.1029/2001JD001225.

——, and Coauthors, 2007: Vertical cloud structure observed from shipborne radar and lidar: Midlatitude case study during the MR01/K02 cruise of the research vessel *Mirai. J. Geophys. Res.*, **112,** D08216, doi:10.1029/2006JD007628.

——, and Coauthors, 2008: Vertical cloud properties in the tropical western Pacific Ocean: Validation of the CCSR/NIES/FRCGC GCM by shipborne radar and lidar. *J. Geophys. Res.*, **113,** D24213, doi:10.1029/2008JD009812.

——, K. Sato, and Y. Hagihara, 2010: Global analysis of ice microphysics from CloudSat and CALIPSO: Incorporation of specular reflection in lidar signals. *J. Geophys. Res.*, **115,** D22209, doi:10.1029/2009JD013383.

Orr, B. W., and R. A. Kropfli, 1999: A method for estimating particle fall velocities from vertically pointing Doppler radar. *J. Atmos. Oceanic Technol.*, **16,** 29–37.

Pruppacher, H. R., and J. D. Klett, 1997: *Microphysics of Clouds and Precipitation.* 2nd ed. Oxford University Press, 914 pp.

Saito, K., and Coauthors, 2006: The operational JMA nonhydrostatic mesoscale model. *Mon. Wea. Rev.*, **134,** 1266–1298.

——, J. Ishida, K. Aranami, T. Hara, T. Segawa, M. Narita, and Y. Honda, 2007: Nonhydrostatic atmospheric models and operational development at JMA. *J. Meteor. Soc. Japan,* **85B,** 271–304.

Sato, K., and H. Okamoto, 2006: Characterization of Z_e and LDR of nonspherical and inhomogeneous ice particles for 95-GHz cloud radar: Its implication to microphysical retrievals. *J. Geophys. Res.*, **111,** D22213, doi:10.1029/2005JD006959.

——, ——, M. K. Yamamoto, S. Fukao, H. Kumagai, Y. Ohno, H. Horie, and M. Abo, 2009: 95-GHz Doppler radar and lidar synergy for simultaneous ice microphysics and in-cloud vertical air motion retrieval. *J. Geophys. Res.,* **114,** D03203, doi:10.1029/2008JD010222.

Satoh, M., T. Inoue, and H. Miura, 2010: Evaluations of cloud properties of global and local cloud-system resolving models using CALIPSO and CloudSat simulators. *J. Geophys. Res.,* **115,** D00H14, doi:10.1029/2009JD012247.

Sekiguchi, M., and T. Nakajima, 2008: A *k*-distribution-based radiation code and its computational optimization for an atmospheric general circulation model. *J. Quant. Spectrosc. Radiat. Transfer,* **109,** 2779–2793, doi:10.1016/j.jqsrt.2008.07.013.

Stephens, G. L., and Coauthors, 2002: The CloudSat mission and the A-Train. *Bull. Amer. Meteor. Soc.,* **83,** 1771–1790.

——, and Coauthors, 2008: The CloudSat mission: Performance and early science after the first year of operation. *J. Geophys. Res.,* **113,** D00A18, doi:10.1029/2008JD009982.

Sugimoto, N., I. Matsui, A. Shimizu, I. Uno, K. Asai, T. Endoh, and T. Nakajima, 2002: Observation of dust and anthropogenic aerosol plumes in the Northwest Pacific with a two-wavelength polarization lidar on board the research vessel *Mirai. Geophys. Res. Lett.,* **29,** 1901, doi:10.1029/2002GL015112.

Takemura, T., T. Nozawa, S. Emori, T. Y. Nakajima, and T. Nakajima, 2005: Simulation of climate response to aerosol direct and indirect effects with aerosol transport-radiation model. *J. Geophys. Res.,* **110,** D02202, doi:10.1029/2004JD005029.

Tanelli, S., S. L. Durden, E. Imm, K. Pak, D. Reinke, P. Partain, J. Haynes, and R. Marchand, 2008: CloudSat's cloud profiling radar after two years in orbit: Performance, calibration, and processing. *IEEE Trans. Geosci. Remote Sens.,* **46,** 3560–3573.

Wilson, D. R., and S. P. Ballard, 1999: A microphysically based precipitation scheme for the UK Meteorological Office Unified Model. *Quart. J. Roy. Meteor. Soc.,* **125,** 1607–1636.